Vacancy-Induced Formation and Growth of Inversion Domains in Transition-Metal Dichalcogenide Monolayer

Junhao Lin,[†,‡] Sokrates T. Pantelides,[†,‡] and Wu Zhou*[,‡]

[†]Department of Physics and Astronomy, Vanderbilt University, Nashville, Tennessee 37235, United States and [‡]Materials Science & Technology Division, Oak Ridge National Laboratory, Oak Ridge, Tennessee 37831, United States

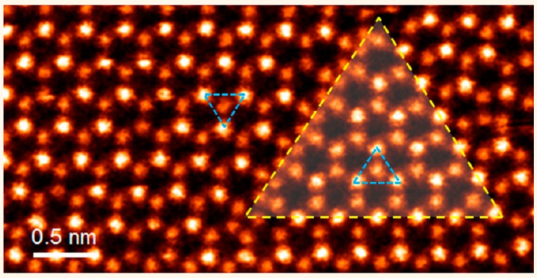

ABSTRACT Sixty degree grain boundaries in semiconducting transition-metal dichalcogenide (TMDC) monolayers have been shown to act as conductive channels that have profound influence on both the transport properties and exciton behavior of the monolayers. Here, we show that annealing TMDC monolayers at high temperature induces the formation of large-scale inversion domains surrounded by such 60° grain boundaries. To study the formation mechanism of such inversion domains, we use the electron beam in a scanning transmission electron microscope to activate the dynamic process within pristine TMDC monolayers. The electron beam acts to generate chalcogen vacancies in TMDC monolayers and provide energy for them to undergo structural evolution. We directly visualize the nucleation and growth of such inversion domains and their 60° grain boundaries atom-by-atom within a $MoSe_2$ monolayer and explore their formation mechanism. Combined with density functional theory, we conclude that the nucleation of the inversion domains and migration of their 60° grain boundaries are driven by the collective evolution of Se vacancies and subsequent displacement of Mo atoms, where such a dynamical process reduces the vacancy-induced lattice shrinkage and stabilizes the system. These results can help to understand the performance of such materials under severe conditions (*e.g.*, high temperature).

KEYWORDS: transition-metal dichalcogenide · vacancy · defect dynamics · inversion domain · grain boundaries

Transition-metal dichalcogenide (TMDC) monolayers are promising candidates for nanoelectronic and optoelectronic applications due to their direct band gap semiconducting nature and strong photoluminescence.[1−4] TMDC monolayers in the 2H phase consist of two distinct elements alternating in the hexagonal honeycomb lattice (Figure 1a), which leads to a threefold rotational symmetry. Therefore, inversion domains (domains of mirror symmetry) emerge when the lattice is rotated by 60°, which equivalently swaps the positions of the metal and chalcogen atoms in the hexagons.[5−9] These inversion domains are connected by 60° grain boundaries (GB) that have been observed as intrinsic defects in chemical vapor deposition (CVD)-grown TMDC monolayers.[5−8] Such 60° GBs are predicted to be metallic,[6,7] acting as conductive channels inside the semiconducting monolayer, and affect both the transport properties and exciton behavior. Experimental studies have shown that a single 60° GB can enhance the in-plane electrical conductivity and drastically quench the local photoluminescence.[8,10] In order to fully develop the potential of TMDC monolayers for device applications, it is important to recognize the possible presence and the dynamics of these metallic 60° GBs in the monolayers. Furthermore, engineering such functional defects within the TMDC monolayer can help to tailor the performance of TMDC monolayers. A recent study showed that 60° GBs in the 2H phase and phase boundaries between 1T/2H phases can be artificially created in a MoS_2 monolayer *via* the synergetic effect of electron irradiation and *in situ* heating.[11] The *in situ* heating generates thermal instability within the lattice, and the high-energy electrons were used to trigger the phase

* Address correspondence to wu.zhou.stem@gmail.com.

Received for review January 25, 2015 and accepted April 23, 2015.

10.1021/acsnano.5b00554

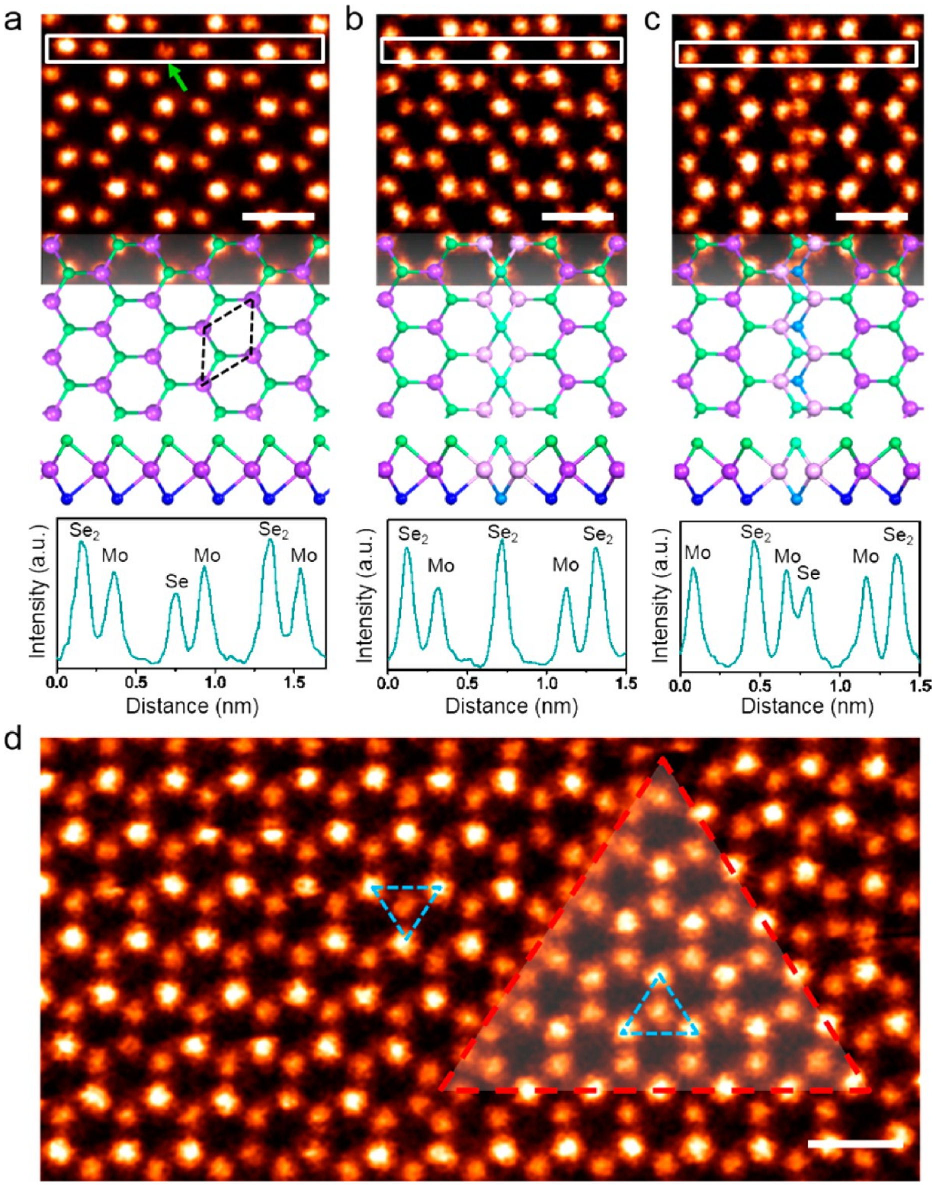

Figure 1. Atomic structure of monoselenium vacancy, 60° grain boundaries, and inversion domain embedded in pristine monolayer $MoSe_2$. (a) High-resolution *Z*-contrast image of the pristine lattice of monolayer $MoSe_2$ with the atomic model overlaid. The green arrow points to a monoselenium vacancy that can be directly identified by its lower contrast as compared to the Se_2 column. The black dashed diamond indicates the unit cell of the pristine lattice. (b,c) *Z*-contrast image and the corresponding structural model of the 4|4P (b) and 4|4E (c) 60° grain boundaries. The side views of all the models are provided below. The line intensity profiles of the monoselenium vacancy and the grain boundaries are provided at the bottom of each panel, respectively. The atoms in the grain boundary regions are highlighted in a slightly different color. (d) Typical triangular inversion domain embedded within the $MoSe_2$ monolayer. Scale bars: 0.5 nm.

transition by electron accumulation.[11,12] Electron irradiation has also been shown to generate chalcogen vacancies and cause their segregation into line defects in TMDC monolayers.[13,14]

In this paper, we first report that thermal annealing a free-standing pristine monolayer MoS_2 alone at an elevated temperature induces the large-scale formation of 60° GBs and inversion domains. Structure and chemical stoichiometry analysis of these 60° GBs indicates that they are chalcogen-deficient. In the second experiment, we use the electron beam in a scanning transmission electron microscope (STEM) to irradiate a pristine $MoSe_2$ monolayer (similar results but with lower image quality were also obtained in MoS_2 monolayer) at room temperature with high electron dose, which intentionally generates and excites Se vacancies within the monolayer and simultaneously monitors their dynamical structural reconstructions *via* sequential *Z*-contrast imaging. We discover that the formation of inversion domains and the 60° GBs within monolayer $MoSe_2$ is indeed induced by the collective evolution of Se vacancies. The Se vacancies preferentially agglomerate into line defects under electron-beam excitation. Such a defect complex subsequently nucleates small triangular inversion domains when Se vacancies are presented at the corner of the line defects, which triggers the Mo sublattice to undergo displacement and continue to expand as more Se vacancies are involved, consistent with our analysis on the growth of the Se-deficient 60° GBs. Density functional theory (DFT) calculations further reveal the driving force for the formation of these inversion domains: the aggregation of Se vacancies induces large lattice shrinkage, which causes the nearby Mo atoms to undergo displacements and nucleate inversion domains in order to release the lattice strain.

RESULTS AND DISCUSSION

Thermal annealing is often involved in the fabrication of monolayer devices.[15,16] We find that annealing an exfoliated free-standing MoS_2 monolayer at an elevated temperature induces high density of triangular inversion domains with size up to 40 nm^2 (details in Supporting Information). These triangular inversion domains have the same 60° GB structures as the intrinsic 60° GBs observed in CVD-grown TMDC monolayers (Figure S1).[5,7] A small amount of oxygen was present during our annealing procedure, which facilitates the formation of sulfur vacancies by decreasing their formation energy (see Supporting Information) and was found to be important for the creation of inversion domains. We noticed that the 60° GB structures generated during our annealing experiment are slightly different from those reported in ref 11 *via* the combination of *in situ* heating and electron irradiation,[11] where no massive loss of atoms was observed during the dynamical process. This indicates that the dynamics and formation mechanism of the 60° GBs and the inversion domain *via* thermal annealing alone may be different from the previous study.[11,12]

Electron irradiation at room temperature on TMDC monolayers generates chalcogen vacancies and provides energy for them to undergo structural evolutions. Structural evolution induced by electron irradiation has been demonstrated as an effective means to explore dynamical processes that span large time scales under typical thermodynamic conditions.[11,14,17−24] In order to study the formation mechanism of the inversion domain and 60° GBs, we performed STEM sequential *Z*-contrast imaging with high electron dose at room temperature on a pristine monolayer $MoSe_2$ sample that has not been annealed at high temperature, as the second experiment. Monolayer $MoSe_2$ was chosen as a representative material of the TMDC family for this study mainly because it has higher threshold against knock-on damage and better image visibility of Se vacancies, which allows for better tracking of the dynamical behavior of Se vacancies. Similar results, but with lower image quality, were also observed in monolayer MoS_2 (Figures S2 and S3). The intensity in *Z*-contrast imaging is related to the atomic number of the imaged species,[25] with the Se_2 columns being brighter than the Mo atoms in a pristine monolayer $MoSe_2$ (Figure 1a). Monoselenium vacancies (V_{Se}) (Figure 1a) and diselenium vacancies (V_{Se_2}) can be distinguished based on their image intensity, as shown in Figure 1. This enables us to directly track the dynamical motions of Se vacancies with single atom sensitivity. As will be shown later, electron irradiation generates the same inversion domains as those obtained by thermal annealing, which suggests that the primary role of the electron beam is to provide energy to overcome the activation barriers; that is, possible charging does not play a significant role as it does in the case of the H-to-T phase transition discussed in ref 11.

A close examination of the atomic structure of the 60° GBs reveals a slight change in chemical stoichiometry as compared to the pristine lattice, suggesting that the creation of such 60° GBs may involve complex motions of vacancies. Figure 1b shows the *Z*-contrast image of a 60° GB containing four-fold rings that share points at Se_2 sites, denoted as 4|4P,[7] where the inversion domain is mirror-symmetric with the original lattice along the GB. Figure 1c shows another type of 60° GB which includes strings of four-fold rings with edge sharing at Mo−Se bonds, denoted as 4|4E,[7] where the inversion domain is shifted by half of the primitive lattice vector along the GB away from the mirror-symmetric positions. At the 4|4P 60° GBs, the Mo atoms retain the six-fold coordination as in a pristine lattice, whereas the coordination of Se atoms with Mo atoms changes from three-fold to four-fold. Similarly, at the 4|4E 60° GBs, the Mo atoms have five-fold coordination instead of six-fold as in the pristine lattice, while Se atoms maintain the same three-fold coordination. The change in coordination alters the local chemical stoichiometry at GB regions, with Mo_4Se_6 ($MoSe_{1.5}$) along the 4|4P 60° GBs and Mo_3Se_5 ($MoSe_{1.67}$) along the 4|4E 60° GBs, when only atoms along the GB with changed bonding conditions are considered. Both GBs show Se deficiency as compared to the pristine $MoSe_2$ stoichiometry. This feature indicates that the formation and expansion of such GBs within the pristine lattice inevitably involve the presence of Se vacancies.[26] Due to the three-fold symmetry of the lattice in $MoSe_2$, the 60° GBs always appear in triangular shapes when created within the pristine monolayer. Ideally, two monoselenium vacancies are needed if the 60° GB expands by one unit cell (details in Figure S4). We note that the GBs participating in the growth of inversion domains have different structure and lower formation energy[27] than the ones observed in ref 28.

Figure 1d shows an inversion domain, produced by prolonged electron irradiation, which contains the two types of 60° GBs described above (see Figure S5 for a

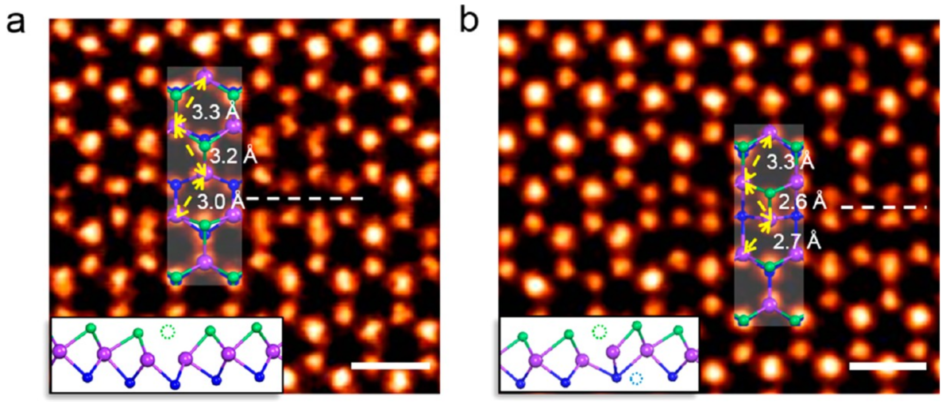

Figure 2. Agglomeration of selenium vacancies into line defects in monolayer $MoSe_2$. (a) STEM *Z*-contrast image of the SL line defect with the DFT-optimized structure overlaid. Inset: Side view of the structure model. The nearby Se_2 columns are slightly misaligned. (b) STEM *Z*-contrast image of the 4|4E GB-like structure (highly strained 4|4E 60° GB) evolved from the SL line defect, which contains deformed strings of four-fold rings. The white dashed lines indicate the centers of these defects, and the yellow dashed arrows highlight the bond length of the Mo sublattice in the defect regions. Scale bars: 0.5 nm.

schematic). The inversion domain is formed from the agglomeration of Se vacancies activated by electron irradiation. Prolonged exposure of the $MoSe_2$ monolayer to electron irradiation generates new Se vacancies,[14,29,30] while the existing ones can also be activated to evolve. Se vacancies are generated mainly *via* ionization damage under our experimental conditions, as the knock-on damage threshold for Se atoms in monolayer $MoSe_2$ is ∼190 kV.[14,30] We found that the formation rate of Se vacancy is proportional to the total electron dose and insensitive to the electron dose rate (Figure S6).

We find that the randomly located Se vacancies can migrate over a few unit cells under the electron excitation, which is due to a low migration barrier (∼2 eV, Figure S7) that can be easily overcome by the energy transferred from the electron beam.[17,30] However, detailed atom-by-atom tracking of the migration process of multiple Se vacancies (Figure S8) reveals that they preferentially agglomerate into lines and reconstruct rather than undergo random walks,[31] as shown in Figure 2a. Such agglomeration of Se vacancies *via* atomic migration leads to the formation of an extended line defect with a single row of Se atoms missing (such structure is abbreviated as SL below), which lowers the energy of the system.[13] Both the experimental image and DFT calculations indicate that the missing Se atoms induce contraction between the remaining Mo atoms along the SL defect due to their unsaturated bonds.

As more Se vacancies nearby continue to migrate into the SL defect, instead of growing longer in length, we observed that the defect complex reconstructs into irregular strings of four-fold rings (abbreviated as 4|4E GB-like structure, which is a highly strained 4|4E 60° GB, as discussed below) and no longer maintains the hexagonal rings (Figure 2b). Such reconstruction is due to the lower formation energy of the 4|4E GB-like structure than the SL defect at a certain critical Se vacancy concentration, as demonstrated in the previous study.[13] Therefore, under continuous electron excitation, the SL defects would more likely develop into the 4|4E GB-like structure than continuously grow in length after reaching the critical length (approximately eight unit cells),[13] as observed in our experiment (Figure S8). The formation of the 4|4E GB-like structure further contracts the surrounding Mo sublattice, as shown by the decreasing Mo–Mo distance (Figure 2b). DFT calculations demonstrate that both the SL defect and the 4|4E GB-like structure show localized metallic behavior (Figure S9).

We find that the nucleation of the inversion domain usually occurs after the accumulation of a certain amount of Se vacancies (∼15 Se vacancies within the nucleation region, Figure S6). Figure 3a–c shows the nucleation process of the inversion domain from the 4|4E GB-like structure. Overlapping images are provided in Figure S10 to illustrate the structural changes in each step. The nucleation was triggered by the Se vacancies generated, either by irradiation damage or migration, at one end of the 4|4E GB-like structure. Figure 3a highlights the region where three Se atoms were removed. The remaining Mo atoms in this region are, therefore, pulled toward each other due to the absence of Se atoms, as highlighted by the dashed rectangle in Figure 3b, leading to local lattice shrinkage. To further estimate such local lattice shrinkage observed in the experiment, we performed DFT calculations in a supercell that contains the defect structure as a function of lattice shrinkage (see Methods in Supporting Information). We used the length ratio *A*/*B* to indicate the lattice shrinkage, where *A* and *B* are the distance between two perpendicular pairs of Mo atoms defined in the deformed regions before and after the nucleation process and the lattice (schematic diagrams in the inset of Figure 4a). We only considered the lattice shrinkage along the armchair direction since the deformation in the 4|4E GB-like structure mainly contracts the lattice in this direction.[13]

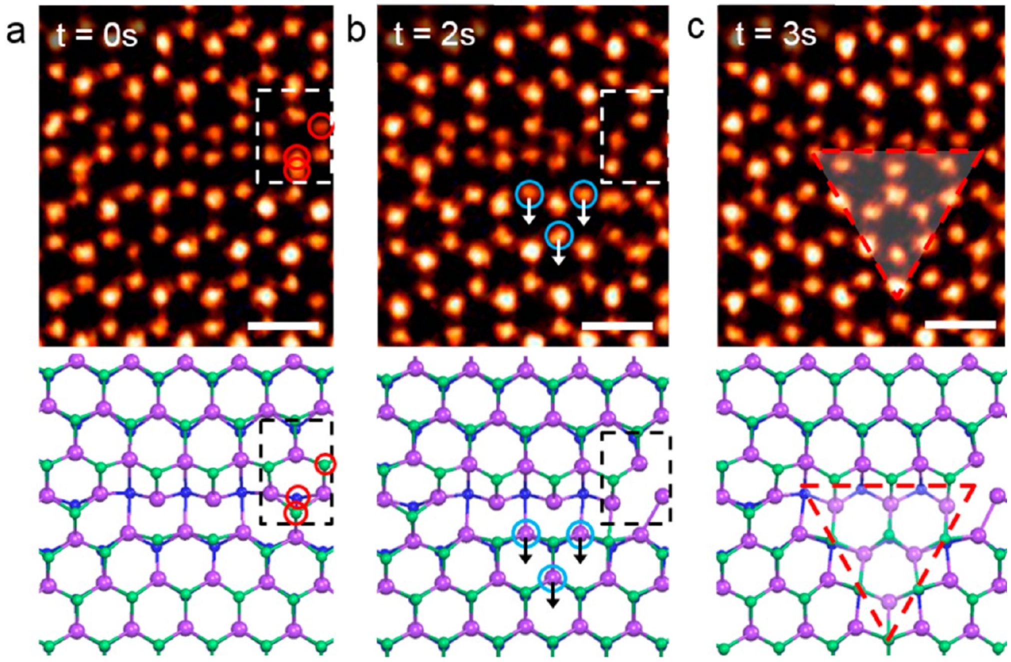

Figure 3. Nucleation of the inversion domain from 4|4E GB-like structure. (a–c) Sequential *Z*-contrast images of the nucleation process. The atomic models are provided below. The dashed rectangles highlight the corner of the defect where Se vacancies are generated, which leads to structural reconstructions. The red circles in (a) highlight the Se atoms that are being removed in the next frame. The arrows in (b) indicate the displacement direction of the Mo atoms during the nucleation of the inversion domain. Scale bars: 0.5 nm.

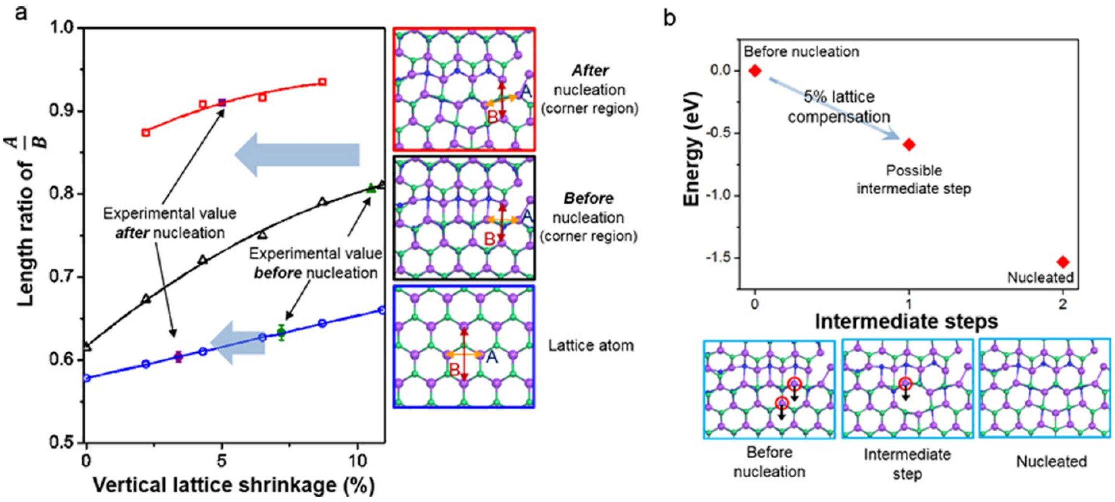

Figure 4. DFT calculations of the nucleation process of the inversion domain. (a) *A*/*B* ratio of Mo sublattice in different regions, where *A* and *B* are defined in the corresponding insets, as a function of lattice shrinkage. The blue, black, and red open symbols are the DFT-calculated values corresponding to the atoms in the lattice (blue) near the 4|4E GB-like structure before (black) and after the nucleation (red). The lines linking the symbols are polynomial fits of the calculated data points. The experimental values are highlighted in green and purple. The error bar of the *A*/*B* ratio of the lattice atoms is the standard deviation from the Mo sublattice close to the defect structure. (b) Energy landscape of the nucleation process. The nucleation of the inversion domain partially releases the local lattice shrinkage and lowers the system energy. Insets: Atomic structure of the possible steps of the nucleation process. The atoms that undergo displacements in each step are highlighted in red circles.

Figure 4a shows the results from the DFT calculations. By fitting the *A*/*B* ratio obtained from the experimental image (Figure 3b,c), we find that the whole 4|4E GB-like structure and its nearby lattice region undergo a large compression prior to the nucleation of the inversion domain, presumably induced by the collective out-of-plane structural reconstructions of the Se vacancies,[13,32] which could make the whole structure unstable. In response to being compressed by the nearby defect, the Mo atoms (in this case, three Mo atoms) can undergo displacements to release the strain (blue circles in Figure 3b). The subsequent reconstructions form two 4|4P 60° GBs and release the strain in the 4|4E GB-like structure, which relaxes

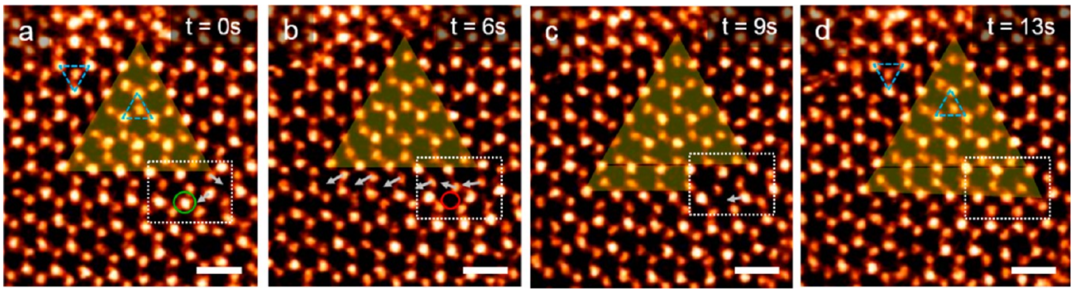

Figure 5. Growth of the inversion domain and migration of the 4|4P 60° grain boundary. (a−d) Sequential STEM *Z*-contrast images of the migration of a 60° grain boundary which leads to the growth of the inversion domain. The dashed rectangle highlights the corner structure of the triangular inversion domain. The green circle in (a) highlights the Se_2 column that is removed in the next frame. The red circle in (b) indicates the as-formed Se vacancy. The white arrows indicate the displacement direction of the atoms. The overlaid yellow triangles indicate the size of the inversion domain. The two dashed blue triangles represent the mirror-symmetric orientations. Scale bars: 0.5 nm.

into a stable 4|4E 60° GB. Due to the three-fold symmetry of the hexagonal $MoSe_2$ lattice, the inversion domain could only be stably formed in a triangular shape within its original lattice. As a consequence, the nucleation of the inversion domain reduces the shrinkage of the lattice and the strain is relaxed after the nucleation (Figure 4a).

Figure 4b depicts the nucleation of the inversion domain in energy landscape. Although the process happens in a time scale that is much faster than the imaging rate (~1 s per frame), the Mo atoms are expected to undergo displacements one after another. The inset in Figure 4b shows a possible intermediate step of the nucleation process. The intermediate step shows that two Mo atoms undergo displacements in the same direction to form a stable eight-membered ring. Such an eight-membered ring is indeed observed during the migration of the 60° GBs (Figure S11). DFT calculations show that such displacement could lower the energy of the system due to the release of the lattice shrinkage. The 5% supercell relaxation for the intermediate state mimics the local relaxation that occurs as indicated in Figure 4a. As a result, calculation of the nucleation barrier is not practical in this case. After the displacement of the remaining Mo atom, the inversion domain formed, which is more stable than the intermediate state. 4|4P and 4|4E 60° GBs (Figure 3c) are formed as a result of the nucleation of the inversion domain. We also find that these two types of 60° GBs can indeed transform into each other *via* shifting half of a unit cell with the presence of Se vacancies nearby (Figure S12).

The 4|4P 60° GBs are observed to migrate more frequently than the other type of GBs under electron-beam excitation. Figures 5 and 6 show a complete migration process of a 4|4P 60° GB, which leads to the growth of the triangular inversion domain. Figure 5a shows the initial state of a triangular inversion domain with three 60° 4|4P GBs. The migration is also found to be initiated by the formation of Se vacancies (highlighted by the green circle in Figure 5a and red circles in Figure 5b after generation of the vacancies) at the corner region of the triangle, which is needed for the expansion of the GBs with Se deficiency. The Se deficiency leads to a slight displacement of the nearby Se column, providing necessary space for the highlighted Mo atom to displace, as illustrated by the arrow in Figure 5a. Such displacement of the Mo atom could then trigger the neighboring Mo atoms in the GB region to undergo displacements along the same direction one by one (Figure 5b). Figure 5d shows the final state after the displacements and corresponding reconstructions, where the inversion domain expands *via* the 60° GB migration. Figure 6c shows an overlapped image between the initial (Figure 6a) and final structure (Figure 6b) for another 60° GB that migrates for one unit cell, elaborating clearly that the expansion of the inversion domain involves a diselenium vacancy, consistent with our stoichiometry analysis (Figure S4). In general, the triangular inversion domain can grow along any of its edges through the same GB migration process (Figure S13).

CONCLUSIONS

In conclusion, we show that the collective evolution of Se vacancies ultimately leads to the formation and growth of inversion domains and their 60° GBs within monolayer $MoSe_2$. We find that Se vacancies tend to first agglomerate into line defect complexes, which subsequently trigger the nucleation of an inversion domain. The growth of such inversion domains occurs *via* the migration of the 60° GBs in the presence of additional Se vacancies. We notice that similar dynamical processes and conclusions were obtained through independent TEM observations very recently.[27] The same vacancy-induced formation and growth of inversion domains can occur during thermal annealing when sufficient thermal energy is supplied to overcome the barrier for the formation and migration of chalcogen vacancies in the TMDC monolayer, as we observed in Figure S1.

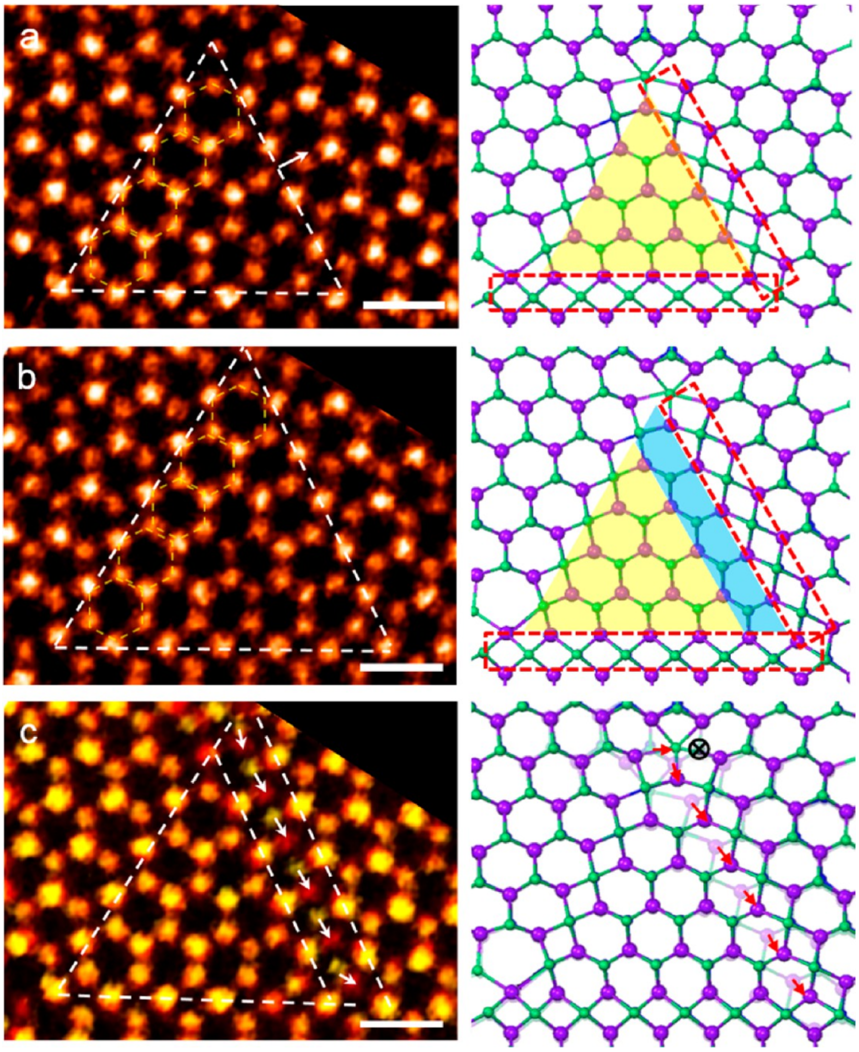

Figure 6. Overlapped image between the initial and final structure of a 4|4P 60° GB migrating for one unit cell. (a,b) *Z*-contrast images of a 4|4P 60° GB before (a) and after (b) migration. The atomic models are provided next to the images. The white dashed lines in the *Z*-contrast images and red dashed rectangles in the atomic models highlight the GB regions. The blue trapezoid in the atomic model indicates the expanded area of the inversion domain. (c) Overlapping of (a) and (b) with different color schemes. The initial image is colorized in yellow, and the final one is in red. The red arrows represent the displacement of the atoms. A diselenium vacancy is needed (indicated by the black circle) for the GB to migrate one unit cell within the pristine lattice. Scale bars: 0.5 nm.

Chalcogen vacancies have been shown to be the most abundant point defect in CVD-grown TMDC monolayers[33] and contribute largely to the transport properties of TMDC-based devices.[34,35] Our study highlights the importance of chalcogen vacancies in the structural stability of TMDC monolayers and the creation of new functional defects. Atomic-level defect engineering in 2D materials is a promising way to tailor the electronic properties of these materials. Our results demonstrate that inversion domains can be obtained at a relatively large scale *via* vacancy engineering. It should be possible in the future to control the choice of nucleation sites of the inversion domains within the material using electron-beam excitation, while the subsequent growth to a specific size is achieved *via* thermal treatment.

METHODS

Sample Preparation and Thermal Annealing Procedure. Monolayer $MoSe_2$ and other TMDC materials were obtained using mechanical exfoliation. The desired layers are then transferred onto gold TEM grids using a routine poly(methyl methacrylate)-free method. High-temperature thermal annealing experiments were only performed on monolayer MoS_2. In the annealing experiment, the gold TEM grid with the free-standing sample was put into a homemade furnace which was connected to a turbo pump. The sample was annealed at 700 °C for 2 h and then taken out for further investigation after it was cooled to room temperature.

STEM *Z*-Contrast Imaging. STEM *Z*-contrast imaging was performed on an aberration-corrected Nion UltraSTEM-100 operating at 100 kV for pristine $MoSe_2$ monolayer samples that had not been annealed at high temperature and at 60 kV for monolayer MoS_2 samples. The convergence semiangle for the incident probe was 31 mrad. The Z-contrast images were gathered for a half-angle range of ∼86−200 mrad. The dwell time for slow single-scan imaging is set to be 12 μs/pixel. The sequential Z-contrast imaging is set to be 1 frame/s, with a dwell time of 4 μs/pixel. All imaging was performed at room temperature.

DFT Calculations. DFT calculations shown in Figure 4 were performed using the Vienna ab initio simulation package[36,37] with the core−valence interaction described by the frozen-core projector-augmented wave method.[38] The exchange-correlation potential was described by the generalized gradient approximation of Perdew−Burke−Ernzerhof.[39] All atoms are allowed to relax until the calculated Hellmann−Feynman force for all atoms is less than 0.01 eV/Å. The shrinkage of the lattice is performed by reducing the lattice vector along the armchair direction of the super cell while keeping the relative position of each atom unchanged.

Conflict of Interest: The authors declare no competing financial interest.

Acknowledgment. We thank Dhiraj Prasai and Dr. Kirill I. Bolotin for helping with the TEM sample preparation, Dave Caudel, Dr. Arnold Burger, Nirmal J. Ghimire, Jiaqiang Yan, and Dr. David G. Mandrus for providing the bulk samples used for mechanical exfoliation, and Dr. Bin Wang for helpful discussions. This research was supported in part by U.S. DOE Grant DE-FG02-09ER46554 (J.L., S.T.P.), by the U.S. Department of Energy, Office of Science, Basic Energy Science, Materials Sciences and Engineering Division (W.Z.), and through a user project supported by ORNL's Center for Nanophase Materials Sciences (CNMS), which is sponsored by the Scientific User Facilities Division, Office of Basic Energy Sciences, U.S. DOE. This research used resources of the National Energy Research Scientific Computing Center, which is supported by the Office of Science of the US Department of Energy under Contract No. DE-AC02-05CH11231.

Supporting Information Available: Figures S1−S13. Discussion of reduced formation energy of sulfur vacancies in MoS_2 with the presence of oxygen molecule. The Supporting Information is available free of charge on the ACS Publications website at DOI: 10.1021/acsnano.5b00554.

REFERENCES AND NOTES

1. Mak, K. F.; Lee, C.; Hone, J.; Shan, J.; Heinz, T. F. Atomically Thin MoS_2: A New Direct-Gap Semiconductor. *Phys. Rev. Lett.* **2010**, *105*, 136805.
2. Radisavljevic, B.; Whitwick, M. B.; Kis, A. Integrated Circuits and Logic Operations Based on Single-Layer MoS_2. *ACS Nano* **2011**, *5*, 9934–9938.
3. Splendiani, A.; Sun, L.; Zhang, Y.; Li, T.; Kim, J.; Chim, C.-Y.; Galli, G.; Wang, F. Emerging Photoluminescence in Monolayer MoS_2. *Nano Lett.* **2010**, *10*, 1271–1275.
4. Geim, A. K.; Grigorieva, I. V. van der Waals Heterostructures. *Nature* **2013**, *499*, 419–425.
5. Lu, X.; Utama, M. I. B.; Lin, J.; Gong, X.; Zhang, J.; Zhao, Y.; Pantelides, S. T.; Wang, J.; Dong, Z.; Liu, Z.; et al. Large-Area Synthesis of Monolayer and Few-Layer $MoSe_2$ Films on SiO_2 Substrates. *Nano Lett.* **2014**, *14*, 2419–2425.
6. Najmaei, S.; Liu, Z.; Zhou, W.; Zou, X.; Shi, G.; Lei, S.; Yakobson, B. I.; Idrobo, J.-C.; Ajayan, P. M.; Lou, J. Vapour Phase Growth and Grain Boundary Structure of Molybdenum Disulphide Atomic Layers. *Nat. Mater.* **2013**, *12*, 754–759.
7. Zhou, W.; Zou, X.; Najmaei, S.; Liu, Z.; Shi, Y.; Kong, J.; Lou, J.; Ajayan, P. M.; Yakobson, B. I.; Idrobo, J.-C. Intrinsic Structural Defects in Monolayer Molybdenum Disulfide. *Nano Lett.* **2013**, *13*, 2615–2622.
8. van der Zande, A. M.; Huang, P. Y.; Chenet, D. A.; Berkelbach, T. C.; You, Y.; Lee, G.-H.; Heinz, T. F.; Reichman, D. R.; Muller, D. A.; Hone, J. C. Grains and Grain Boundaries in Highly Crystalline Monolayer Molybdenum Disulphide. *Nat. Mater.* **2013**, *12*, 554–561.
9. Zou, X.; Liu, Y.; Yakobson, B. I. Predicting Dislocations and Grain Boundaries in Two-Dimensional Metal-Disulfides from the First Principles. *Nano Lett.* **2013**, *13*, 253–258.
10. Najmaei, S.; Amani, M.; Chin, M. L.; Liu, Z.; Birdwell, A. G.; O'Regan, T. P.; Ajayan, P. M.; Dubey, M.; Lou, J. Electrical Transport Properties of Polycrystalline Monolayer Molybdenum Disulfide. *ACS Nano* **2014**, *8*, 7930–7937.
11. Lin, Y.-C.; Dumcenco, D. O.; Huang, Y.-S.; Suenaga, K. Atomic Mechanism of the Semiconducting-to-Metallic Phase Transition in Single-Layered MoS_2. *Nat. Nanotechnol.* **2014**, *9*, 391–396.
12. Kan, M.; Wang, J. Y.; Li, X. W.; Zhang, S. H.; Li, Y. W.; Kawazoe, Y.; Sun, Q.; Jena, P. Structures and Phase Transition of a MoS_2 Monolayer. *J. Phys. Chem. C* **2014**, *118*, 1515–1522.
13. Komsa, H.-P.; Kurasch, S.; Lehtinen, O.; Kaiser, U.; Krasheninnikov, A. V. From Point to Extended Defects in Two-Dimensional MoS_2: Evolution of Atomic Structure under Electron Irradiation. *Phys. Rev. B* **2013**, *88*, 035301.
14. Komsa, H.-P.; Kotakoski, J.; Kurasch, S.; Lehtinen, O.; Kaiser, U.; Krasheninnikov, A. V. Two-Dimensional Transition Metal Dichalcogenides under Electron Irradiation: Defect Production and Doping. *Phys. Rev. Lett.* **2012**, *109*, 035503.
15. Radisavljevic, B.; Radenovic, A.; Brivio, J.; Giacometti, V.; Kis, A. Single-Layer MoS_2 Transistors. *Nat. Nanotechnol.* **2011**, *6*, 147–150.
16. Nan, H.; Wang, Z.; Wang, W.; Liang, Z.; Lu, Y.; Chen, Q.; He, D.; Tan, P.; Miao, F.; Wang, X.; et al. Strong Photoluminescence Enhancement of MoS_2 through Defect Engineering and Oxygen Bonding. *ACS Nano* **2014**, *8*, 5738–5745.
17. Lee, J.; Zhou, W.; Pennycook, S. J.; Idrobo, J.-C.; Pantelides, S. T. Direct Visualization of Reversible Dynamics in a Si_6 Cluster Embedded in a Graphene Pore. *Nat. Commun.* **2013**, *4*, 1650.
18. Li, C.; Wu, Y.; Pennycook, T. J.; Lupini, A. R.; Leonard, D. N.; Yin, W.; Paudel, N.; Al-Jassim, M.; Yan, Y.; Pennycook, S. J. Carrier Separation at Dislocation Pairs in CdTe. *Phys. Rev. Lett.* **2013**, *111*, 096403.
19. Susi, T.; Kotakoski, J.; Kepaptsoglou, D.; Mangler, C.; Lovejoy, T. C.; Krivanek, O. L.; Zan, R.; Bangert, U.; Ayala, P.; Meyer, J. C.; et al. Silicon-Carbon Bond Inversions Driven by 60-keV Electrons in Graphene. *Phys. Rev. Lett.* **2014**, *113*, 115501.
20. Cretu, O.; Krasheninnikov, A. V.; Rodríguez-Manzo, J. A.; Sun, L.; Nieminen, R. M.; Banhart, F. Migration and Localization of Metal Atoms on Strained Graphene. *Phys. Rev. Lett.* **2010**, *105*, 196102.
21. Kotakoski, J.; Krasheninnikov, A. V.; Kaiser, U.; Meyer, J. C. From Point Defects in Graphene to Two-Dimensional Amorphous Carbon. *Phys. Rev. Lett.* **2011**, *106*, 105505.
22. Cretu, O.; Komsa, H.-P.; Lehtinen, O.; Algara-Siller, G.; Kaiser, U.; Suenaga, K.; Krasheninnikov, A. V. Experimental Observation of Boron Nitride Chains. *ACS Nano* **2014**, *8*, 11950–11957.
23. Girit, Ç. Ö.; Meyer, J. C.; Erni, R.; Rossell, M. D.; Kisielowski, C.; Yang, L.; Park, C.-H.; Crommie, M. F.; Cohen, M. L.; Louie, S. G.; et al. Graphene at the Edge: Stability and Dynamics. *Science* **2009**, *323*, 1705–1708.
24. Chen, J. H.; Autès, G.; Alem, N.; Gargiulo, F.; Gautam, A.; Linck, M.; Kisielowski, C.; Yazyev, O. V.; Louie, S. G.; Zettl, A. Controlled Growth of a Line Defect in Graphene and Implications for Gate-Tunable Valley Filtering. *Phys. Rev. B* **2014**, *89*, 121407.
25. Krivanek, O. L.; Chisholm, M. F.; Nicolosi, V.; Pennycook, T. J.; Corbin, G. J.; Dellby, N.; Murfitt, M. F.; Own, C. S.; Szilagyi, Z. S.; Oxley, M. P.; et al. Atom-by-Atom Structural and Chemical Analysis by Annular Dark-Field Electron Microscopy. *Nature* **2010**, *464*, 571–574.
26. Zou, X.; Yakobson, B. I. An Open Canvas—2D Materials with Defects, Disorder, and Functionality. *Acc. Chem. Res.* **2015**, *48*, 73–80.
27. Lehtinen, O.; Komsa, H.-P.; Pulkin, A.; Whitwick, M. B.; Chen, M.-W.; Lehnert, T.; Mohn, M. J.; Yazyev, O. V.; Kis, A.; Kaiser, U.; et al. Atomic Scale Microstructure and Properties of Se-Deficient Two-Dimensional $MoSe_2$. *ACS Nano* **2015**, *9*, 3274–3283.

28. Liu, H.; Jiao, L.; Yang, F.; Cai, Y.; Wu, X.; Ho, W.; Gao, C.; Jia, J.; Wang, N.; Fan, H.; et al. Dense Network of One-Dimensional Midgap Metallic Modes in Monolayer $MoSe_2$ and Their Spatial Undulations. *Phys. Rev. Lett.* **2014**, *113*, 066105.
29. Liu, X.; Xu, T.; Wu, X.; Zhang, Z.; Yu, J.; Qiu, H.; Hong, J.-H.; Jin, C.-H.; Li, J.-X.; Wang, X.-R.; et al. Top-Down Fabrication of Sub-nanometre Semiconducting Nanoribbons Derived from Molybdenum Disulfide Sheets. *Nat. Commun.* **2013**, *4*, 1776.
30. Lin, J.; Cretu, O.; Zhou, W.; Suenaga, K.; Prasai, D.; Bolotin, K. I.; Cuong, N. T.; Otani, M.; Okada, S.; Lupini, A. R.; et al. Flexible Metallic Nanowires with Self-Adaptive Contacts to Semiconducting Transition-Metal Dichalcogenide Monolayers. *Nat. Nanotechnol.* **2014**, *9*, 436–442.
31. Kotakoski, J.; Mangler, C.; Meyer, J. C. Imaging Atomic-Level Random Walk of a Point Defect in Graphene. *Nat. Commun.* **2014**, *5*, 3991.
32. Azizi, A.; Zou, X.; Ercius, P.; Zhang, Z.; Elías, A. L.; Perea-López, N.; Stone, G.; Terrones, M.; Yakobson, B. I.; Alem, N. Dislocation Motion and Grain Boundary Migration in Two-Dimensional Tungsten Disulphide. *Nat. Commun.* **2014**, *5*, 4867.
33. Hong, J.; Hu, Z.; Probert, M.; Li, K.; Lv, D.; Yang, X.; Gu, L.; Mao, N.; Feng, Q.; Xie, L.; et al. Exploring Atomic Defects in Molybdenum Disulphide Monolayers. *Nat. Commun.* **2015**, *6*, 6293.
34. Yuan, S.; Roldán, R.; Katsnelson, M. I.; Guinea, F. Effect of Point Defects on the Optical and Transport Properties of MoS_2 and WS_2. *Phys. Rev. B* **2014**, *90*, 041402.
35. Qiu, H.; Xu, T.; Wang, Z.; Ren, W.; Nan, H.; Ni, Z.; Chen, Q.; Yuan, S.; Miao, F.; Song, F.; et al. Hopping Transport through Defect-Induced Localized States in Molybdenum Disulphide. *Nat. Commun.* **2013**, *4*, 2642.
36. Kresse, G.; Furthmüller, J. Efficiency of *Ab-Initio* Total Energy Calculations for Metals and Semiconductors Using a Plane-Wave Basis Set. *Comput. Mater. Sci.* **1996**, *6*, 15–50.
37. Kresse, G.; Hafner, J. *Ab Initio* Molecular Dynamics for Liquid Metals. *Phys. Rev. B* **1993**, *47*, 558–561.
38. Blöchl, P. E. Projector Augmented-Wave Method. *Phys. Rev. B* **1994**, *50*, 17953–17979.
39. Perdew, J. P.; Burke, K.; Ernzerhof, M. Generalized Gradient Approximation Made Simple. *Phys. Rev. Lett.* **1996**, *77*, 3865–3868.